applied sciences

MDPI

Article

Design and Implementation of a Six-Degrees-of-Freedom Underwater Remotely Operated Vehicle

Khaled M. Salem [1], Mohammed Rady [2,*], Hesham Aly [3] and Haitham Elshimy [4,5]

[1] Department of Basic and Applied Science Engineering, Arab Academy for Science, Technology and Maritime Transport (Smart Village Campus), Smart Village, Giza 12577, Egypt; khaled.selem1997@adj.aast.edu
[2] Construction and Building Engineering Department, College of Engineering and Technology, Arab Academy for Science, Technology and Maritime Transport (AASTMT), B 2401 Smart Village, Giza 12577, Egypt
[3] Department of Electronics and Communication Engineering, Arab Academy for Science, Technology and Maritime Transport (Smart Village Campus), Smart Village, Giza 12577, Egypt; hesham_aly@aast.edu
[4] Department of Mechanical and Aerospace Engineering, United Arab Emirates University, Al Ain 15551, United Arab Emirates; haithamelshimy@uaeu.ac.ae or haitham.elshimy@nsst.bsu.edu.eg
[5] Department of Space Navigation, Faculty of Navigation Science and Space Technology, Beni Suef University, Beni Suef 62521, Egypt
* Correspondence: mohammed.radhy@aast.edu

Abstract: In recent decades, there has been considerable interest in developing underwater remotely operated vehicles (ROVs) due to their vital role in exploring ocean depths to perform missions in various applications, including offshore oil and gas, military and defense, scientific research, and aquaculture. To this end, researchers must consider multiple aspects to develop ROVs, such as general design, power and thrust system, navigation and control, and obstacle avoidance. Accordingly, this paper proposes an integrated framework for designing and implementing an ROV prototype, considering the mechanical, electrical, and software systems. Eventually, image processing was implemented using Python to examine the ROV's capabilities in performing underwater missions. The proposed design employs six thrusters to provide controllability of the ROV in six-degrees-of-freedom (DOF). We coated the track width of the printed circuit board (PCB) with a composite mixture of tin, silver, and gold to resist corrosion and harsh environments, enhance the circuit performance and solderability, and increase its life span. The PCB was designed to sustain 30 A with 10 cm × 10 cm dimensions. The image processing results revealed that the proposed ROV could successfully identify the benthic species, follow the desired routes, detect cracks, and analyze obstacles.

Keywords: ROV; ocean robotics; underwater detection; marine; image processing; sensors

Citation: Salem, K.M.; Rady, M.; Aly, H.; Elshimy, H. Design and Implementation of a Six-Degrees-of-Freedom Underwater Remotely Operated Vehicle. *Appl. Sci.* **2023**, *13*, 6870. https://doi.org/10.3390/app13126870

Academic Editor: Yudong Zhang

Received: 14 May 2023
Revised: 28 May 2023
Accepted: 2 June 2023
Published: 6 June 2023

1. Introduction

The water surface covers almost three-fourths of our planet's total surface area, providing humans with a variety of mineral and natural resources. With terrestrial reserves being depleted, a growing focus has arisen on exploring the seabed for resources such as gas, oil, and minerals. However, traditional manned systems and human divers are limited in investigating vast and often hazardous underwater environments. To overcome these challenges, remotely operated vehicles (ROVs) have gained popularity among governmental agencies and commercial companies as they can undertake complex missions without risking human lives [1]. ROVs are often equipped with cameras, sensors, and manipulator's arms, allowing operators to remotely navigate and interact with the underwater environment [2–6]. They are operated from a surface vessel or a control room onshore, using a tether that provides power and communication between the vehicle and the operator. ROVs have revolutionized how we explore the ocean, allowing us to gather data and samples, perform maintenance and repairs on underwater infrastructure, and conduct scientific research in inaccessible areas [7–10].

Ali et al. [11] developed a twin-controller approach using Matlab to regulate the behavior of underwater ROVs. The controller design comprises proportional-integral-derivative (PID) to tune the adaptive gains of the aquatic system and model reference adaptive control (MRAC) to mitigate the dynamic system's disturbance. Dong et al. [12] proposed a depth control strategy that combines fuzzy PID and dynamic compensation. Using ANSYS, the hydrodynamics analysis of ROV was conducted to find out the relationship between the resistance of water and moving velocity in the heave direction. The depth control can vary by 3 cm, which is practical for the reactor pool.

Bykanova et al. [13] developed a small-sized ROV for shipwrecks with a variable storing moment by rotating the wing in the vehicle's plane. The ROV had four horizontal thrusters to increase the range of maneuverability. Furthermore, the ROV was enhanced with a lithium battery to reduce the tether's weight and return to the coast in case of emergency or damage to the cable.

Omerdic et al. [14] designed a prototype platform to test and validate new technologies for marine operations. The designed ROV was equipped with advanced 3D visual displays, an easy pilot interface, voice control navigation, and low-level controllers with an autotuning system. The position of a fully actuated underwater ROV with a manipulator was stabilized by Ali et al. [9]. They applied the proposed control algorithm on an eight degrees-of-freedom (DOF) ROV to control the erratic deviations. The simulations proved that the designed ROV could effectively reach the desired position.

Other researchers assessed different control methods using neural networks, demonstrating their benefits, shortcomings, and applications [15,16]. Caccia and Veruggio [17] developed an ROV navigation system through pre-programmed controllers to control the speed. Do et al. [18] designed an adaptive control mechanism to ensure a 6-DOF ROV follows the desired route. Hoang and Kreuzer [19] proposed a hybrid PID controller for the dynamic orientation of ROVs to ensure the accurate execution of tasks near underwater structures.

Despite the efforts of previous researchers to enhance the performance of ROVs, little attention has been paid to integrating the various phases of design and fabrication. Thus, the main objective of this study is to develop an entire framework that considers the design, manufacturing, and assembling of a portable ROV system. Furthermore, a coating technique of track width in the printed circuit board (PCB) is presented to reduce the size of the electrical enclosure and, consequently, the vehicle's size. Subsequently, an image processing technique is developed to enhance the ROV's capabilities for performing various tasks in underwater environments. This paper is arranged as follows: Section 1 provides a background and literature survey, Section 2 presents the mathematical model of ROV, Section 3 illustrates the mechanical design structure, Section 4 discusses the electrical system design, Section 5 presents the software system, Section 6 presents the experimental setup, Section 7 presents the results and discussion, and finally, Section 8 presents the conclusions, limitations, and recommendations for future work.

2. Mathematical Model

2.1. Assumptions

The ROV's dynamic model is complex and requires several parameters. Hence, the present study considered the following assumptions to simplify the mathematical model [4].

- The ROV is symmetrical about its 3 planes.
- The center of buoyancy of the ROV is located on the geometric symmetry plane.
- The ROV was simulated as a rigid body; therefore, no geometrical and bending deformations were considered.
- The ROV's hydrodynamic coefficients were not variable.

2.2. Coordinate System

The analysis of the kinematic and kinetic models is a part of the ROV's modeling. To create the six-DOF nonlinear dynamics model of the ROV, we first introduced the

coordinate system and specifications of its motion parameters based on two reference coordinate systems (Figure 1).

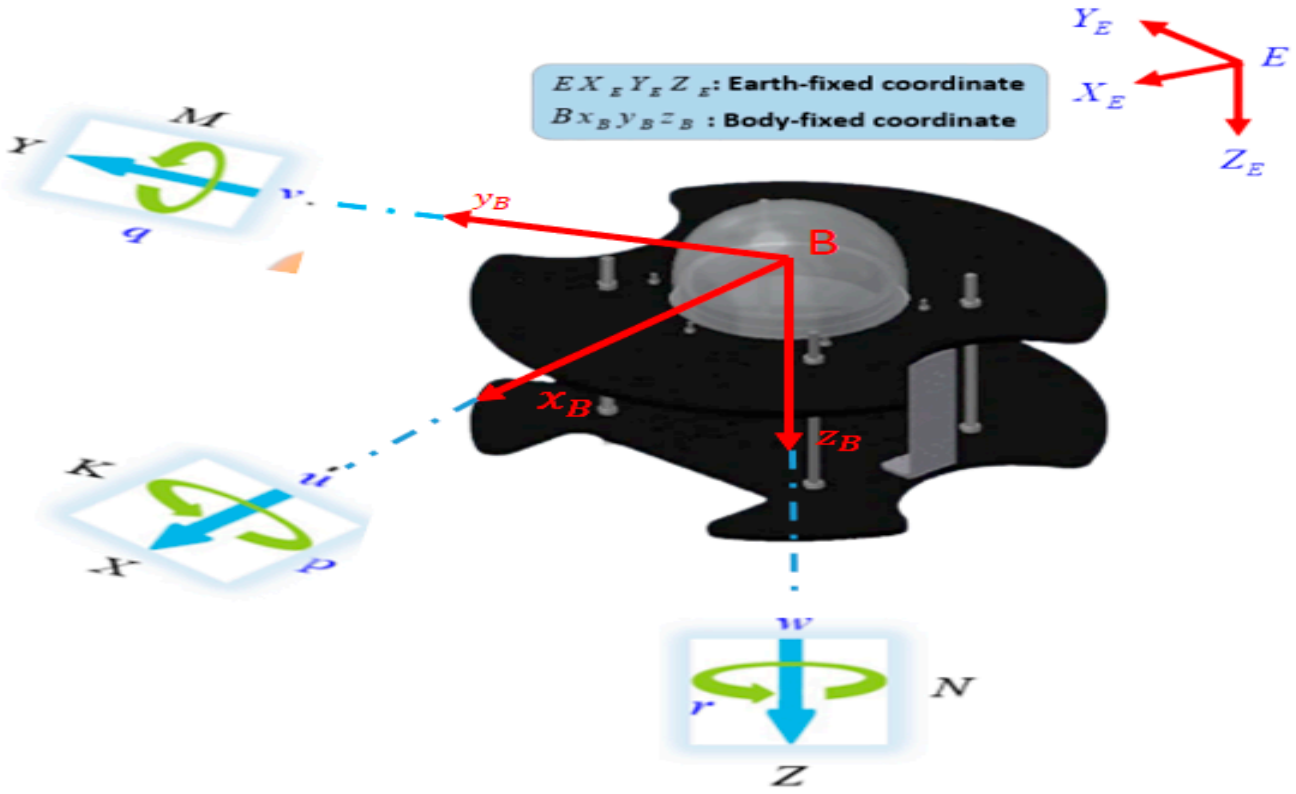

Figure 1. The underwater ROV coordinate system.

The ROV has two vertical thrusters and four horizontal thrusters. Thus, the following state vectors are utilized with the six-DOF equation of motion [20,21]: $\eta = \begin{bmatrix}\eta_1^T & \eta_2^T\end{bmatrix}^T$ illustrates the linear positions and Euler angles vector of the ROV in the earth-fixed (EF) frame $E - X_E Y_E Z_E$, an explanation of the linear position $\eta_1 = [x, y, z]^T$ and the angular position $\eta_2 = [\phi, \theta, \psi]^T$; The ROV's linear position is indicated by the letters x, y, and z; $\varphi, \theta,$ and ψ, roll, pitch, and yaw, three Euler angles, respectively; $v = \begin{bmatrix}v_1^T & v_2^T\end{bmatrix}^T$ represents the velocities vector in the body-fixed (BF) frame $B - XYZ$, explaning the linear velocity $v_1 = [u, v, w]^T$ and the angular velocity $v_2 = [p, q, r]^T$.

2.3. Kinematic Equations

Since two coordinate systems are utilized in the ROV model, a coordinate transformation matrix is used to transfer the ROV's motion representation from the BF frame to the EF frame or vice versa. Hence, the kinematic equations for an ROV are expressed as follows:

$$\dot{\eta}_1 = J_1(\eta_2)v_1 \tag{1}$$

$$\dot{\eta}_2 = J_2(\eta_2)v_2 \tag{2}$$

$$J_1(\eta_2) = \begin{bmatrix} c\psi c\theta & -s\psi c\phi + s\phi s\theta c\psi & s\psi s\phi + s\theta c\psi c\phi \\ s\psi c\theta & c\psi c\phi + s\phi s\theta s\psi & -c\psi s\phi + s\theta s\psi c\phi \\ -s\theta & s\phi c\theta & c\phi c\theta \end{bmatrix} \tag{3}$$

$$J_2(\eta_2) = \begin{bmatrix} 1 & \mathrm{s}\phi\mathrm{t}\theta & \mathrm{c}(\phi)\mathrm{t}\theta \\ 0 & \mathrm{c}\phi & -\mathrm{s}\phi \\ 0 & \mathrm{s}\phi/\mathrm{c}\theta & \mathrm{c}\phi/\mathrm{c}\theta \end{bmatrix} \tag{4}$$

where s, c, and t denote sin, cos, and tan, respectively.

2.4. Kinetic Equations

Generally, the ROV's motion is represented by the six-DOF nonlinear equation. Here, the following is a matrix representation of the nonlinear dynamic of the ROV in the BF frame [22]:

$$M\dot{v} + C(v)v + D(v)v + G(\eta) = \tau + \tau_d \tag{5}$$

where M is the global inertial matrix, $C(v)$ denotes the coriolis and centripetal matrix, $D(v)$ denotes the damping matrix, $G(\eta)$ denotes the matrix of restoring force and moments, τ denotes the thruster forces and moments, and τ_d denotes the external disturbance forces and moments.

2.4.1. Inertial Matrix

The global inertial matrix refers to the sum of the ROV's inertial matrix M_{RB} and an additional hydrodynamic inertial matrix M_A due to the surrounding fluid's inertial (Equations (6)–(8)).

$$M = M_{RB} + M_A \in R^{6\times 6} \tag{6}$$

$$M_{RB} = \begin{bmatrix} m & 0 & 0 & 0 & mz_{\mathrm{G}} & -my_{\mathrm{G}} \\ 0 & m & 0 & -mz_{\mathrm{G}} & 0 & mx_{\mathrm{G}} \\ 0 & 0 & m & my_{\mathrm{G}} & -mx_{\mathrm{G}} & 0 \\ 0 & -mz_{\mathrm{G}} & my_{\mathrm{G}} & I_{xx} & I_{xy} & I_{xz} \\ mz_{\mathrm{G}} & 0 & -mx_{\mathrm{G}} & I_{yx} & I_{yy} & I_{yz} \\ -my_{\mathrm{G}} & mx_{\mathrm{G}} & 0 & I_{zx} & I_{zy} & I_{zz} \end{bmatrix} \tag{7}$$

$$M_A = \begin{bmatrix} X_{i\dot{u}} & 0 & 0 & 0 & 0 & 0 \\ 0 & Y_{\dot{v}} & 0 & 0 & 0 & Y_{\dot{r}} \\ 0 & 0 & Z_{\dot{w}} & 0 & Z_{\dot{q}} & 0 \\ 0 & 0 & 0 & K_{\dot{p}} & 0 & 0 \\ 0 & 0 & M_{\dot{w}} & 0 & M_{\dot{q}} & 0 \\ 0 & N_{\dot{v}} & 0 & 0 & 0 & N_{\dot{r}} \end{bmatrix} \tag{8}$$

where m stands for the mass of the ROV; x_G, y_G, and z_G denote the mass center of the ROV, respectively; and I_{ij} is the inertia tensor for each axis of subscripts.

2.4.2. Coriolis and Centripetal Matrix

The Coriolis and centripetal matrix refers to the sum of a rigid-body Coriolis and the ROV's centripetal matrix $C_{RB}(v)$ and an added-mass Coriolis and centripetal matrix C_A (Equations (9)–(11)).

$$C(v) = C_{RB}(v) + C_A(v) \in R^{6\times 6} \tag{9}$$

$$C_{RB}(v) = \begin{bmatrix} 0 & 0 & 0 \\ 0 & 0 & 0 \\ 0 & 0 & 0 \\ -m(y_G q + z_G r) & m(y_G q + w) & m(z_G p - v) \\ m(x_G q - w) & -m(z_G r + x_G p) & m(z_G q + u) \\ m(x_G r + v) & m(y_G r - u) & -m(x_G p + y_G q) \end{bmatrix}$$

$$\begin{matrix} m(y_G q + z_G r) & -m(x_G q - w) & -m(x_G r + v) \\ -m(y_G q + w) & m(z_G r + x_G p) & -m(y_G r - u) \\ -m(z_G p - v) & -m(z_G q + u) & m(x_G p + y_G q) \\ -m(z_G p - v) & -m(z_G q + u) & m(x_G p + y_G q) \\ 0 & -I_{yz} q - I_{xz} p + I_{zz} r & I_{yz} r + I_{xy} p - I_{yy} q \\ I_{yz} q + I_{xz} p - I_{zz} r & 0 & -I_{xz} r - I_{xy} q + I_{xx} p \\ -I_{yz} r - I_{xy} p + I_{yy} q & I_{xz} r + I_{xy} q - I_{xx} p & 0 \end{matrix} \begin{bmatrix} \\ \\ \\ \\ \\ \\ \\ \end{bmatrix} \quad (10)$$

$$C_A(v) = -\begin{bmatrix} 0 & 0 & 0 & 0 & -Z_{\dot{w}} w & Y_{\dot{v}} v \\ 0 & 0 & 0 & Z_{\dot{w}} w & 0 & -X_{\dot{u}} u \\ 0 & 0 & 0 & -Y_{\dot{v}} v & X_{\dot{u}} u & 0 \\ 0 & -Z_{\dot{w}} w & Y_{\dot{v}} v & 0 & -N_{\dot{r}} r & M_{\dot{q}} q \\ Z_{\dot{w}} w & 0 & -X_{\dot{u}} u & N_{\dot{r}} r & 0 & -K_{\dot{p}} p \\ -Y_{\dot{v}} v & X_{\dot{u}} u & 0 & -M_{\dot{q}} q & K_{\dot{p}} p & 0 \end{bmatrix} \quad (11)$$

2.4.3. Damping Matrix

The ROV's damping matrix in the fluid $D(v) \in R^{6\times 6}$, which consists of the force and the moment of the first and second-order velocities, can be represented as follows:

$$D(v) = -\text{diag}\{X_u, Y_v, Z_w, K_p, M_q, N_r\} - \text{diag}\left\{X_{u|u|}\left|u\right|, Y_{v|v|}\left|v\right|, Z_{w|w|}\left|w\right|, K_{p|p|}\left|p\right|, M_{q|q|}\left|q\right|, N_{r|r|}\left|r\right|\right\} \quad (12)$$

2.4.4. Restoring Forces and Moments

Considering the center of buoyancy of the ROV, as stated in the BF frame is $[x_b, 0, x_z]^T$, the restoring forces and moments $G(\eta) \in R^{6\times 1}$ could be expressed as follows [21,23]:

$$G(\eta) = \begin{bmatrix} (W - B)\sin\theta \\ -(W - B)\cos\theta\sin\phi \\ -(W - B)\cos\theta\cos\phi \\ -(y_G W - y_b B)\cos\theta\cos\phi + (z_G W - z_b B)\cos\theta\sin\phi \\ (z_G W - z_b B)\sin\theta + (x_G W - x_b B)\cos\theta\cos\phi \\ -(x_G W - x_b B)\cos\theta\sin\phi - (y_G W - y_b B)\sin\theta \end{bmatrix} \quad (13)$$

where W and B represent the gravity force and the buoyancy force, respectively.

3. Mechanical Design Structure

The proposed mechanical design should provide an easy-to-assemble, lightly weighted, and maneuverable ROV capable of performing tasks efficiently in a reasonable time. Accordingly, we sought a balance between high performance and innovative design of ROV [22].

3.1. Structure of ROV

There are three phases to build the structure of ROV. Firstly, in the brainstorming phase, various free-hand sketches have been drawn, edited, and discussed to reach an efficient design for ROV. Subsequently, the design that could meet the electrical requirements was chosen. Accordingly, we designed our ROV in a circular shape to allow easy rotational

movement, smoothness of motion, and reduction in turbulent flow. The curvature in the electrical enclosure enables the reduction in drag force due to the streamlined shape.

Several computer-aided design (CAD) programs were utilized for the design process. Inventor was used for simulating the solid model and assemblage of ROV. AutoCAD was used for preparing the final files of ROV for printing and fabrication. At the end of the two phases, we discussed the materials based on the calculations and costs of the suggested materials for ROV's upper plate, lower plate, and electrical enclosure. Figure 2 illustrates the ROV's structure.

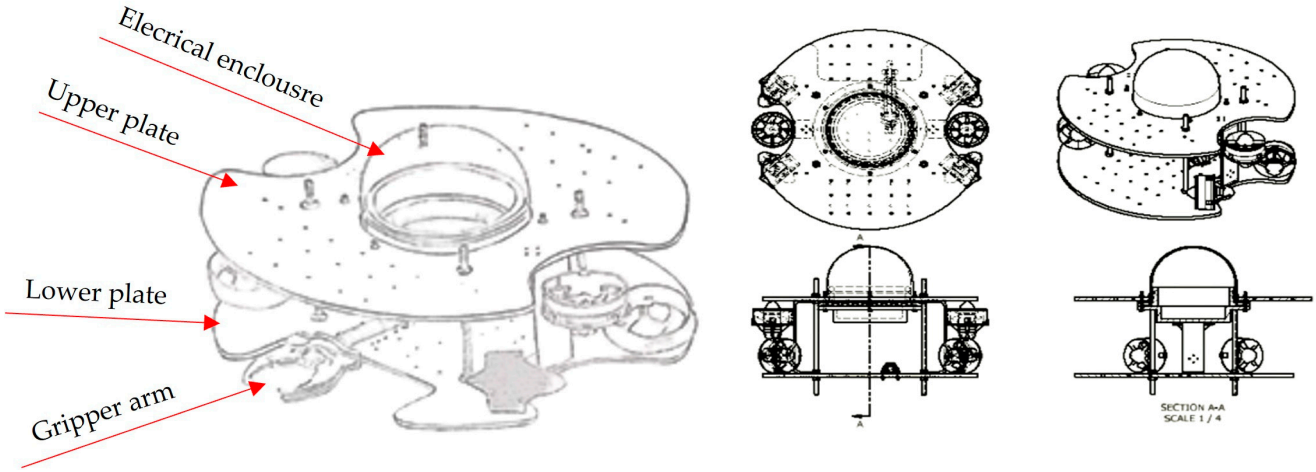

(**a**) (**b**)

Figure 2. (**a**) First phase: free hand-sketch, (**b**) Final CAD views for ROV prototype.

3.2. Material Selection

Selecting materials for an ROV depends on various factors, such as the intended use of the ROV, operating conditions, budget, and performance requirements. The ROV consists of upper and lower plates held together by four shafts. The electronic enclosure is connected to the upper plate via six bolts, and the lower plate is for the four horizontal thrusters. Two cameras were installed on the ROV. The upper and lower plates were made of acrylic with 10 thicknesses to resist corrosion and ease manufacturing. The electric housing dome was also made of acrylic due to its light transmittance, ability to withstand water pressure, and ease of insulation.

Stainless steel was chosen for shafts, rivets, washers, and nuts because of its ability to resist corrosion under water. Additionally, it can withstand high strength and power. Two holders were placed for the vertical thrusters between the two plates. Many screw holes were located on the upper and lower plates to enable easy installation of tools in the plates and for motor positioning. Figure 3 illustrates the developed prototype.

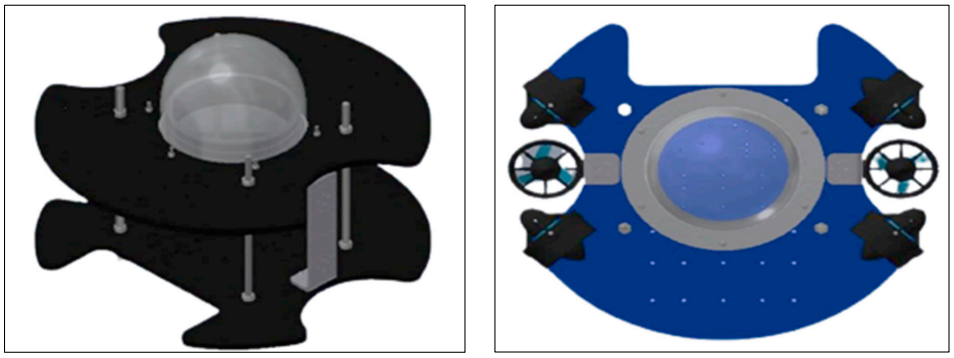

(**a**) (**b**)

Figure 3. Proposed ROV prototype (**a**) Isometric view, (**b**) Top view.

3.3. Configuration of Thrusters

We calculated the maximum force to move our vehicle up and down to choose the suitable type of thruster and determine whether the thrusters could dive. We used six Blue-robotics T100 thrusters. Compared to bilge pumps, they have a greater thrust-to-physical size ratio [6]. Accordingly, they can provide more free space to install the mechanisms required for the required tasks. However, the T100 thrusters have a high-power consumption at high-speed operations. Equation (14) expresses the computation of the drag force D:

$$D = 0.5A\rho V^2 C_d \tag{14}$$

where D is the drag force, A is the ROV's cross-sectional area, ρ is the fluid's density, V is the object's speed relative to the fluid, and C_d is the drag coefficient.

According to Equation (14), to achieve suitable maneuverability and to introduce lateral translation, four equally spaced thrusters were located on a prevalent plane and were vectored at 45° angles in the corners as shown in Figure 4a. The two motors were in front of ROV (a forward position), and the two thrusters were in the back of ROV (a backward position). Two vertical thrusters were installed on the vehicle's right and left sides. As a result, the vehicle could achieve six-DOF (namely, Surge, Sway, Heave, Yaw, Roll, Pitch). The 6-DOF of the ROV is illustrated in Figure 4b.

This configuration allows the thrusters to contribute to the power efficiently towards better propulsion. It also reduces flow interference, considering the overcoming drag that might interrupt the vehicle and the drag of the tether. Each blue-robotics T100 thruster has a maximum forward thruster = 23.15 N and a maximum backward thruster = 17.85 N [24,25].

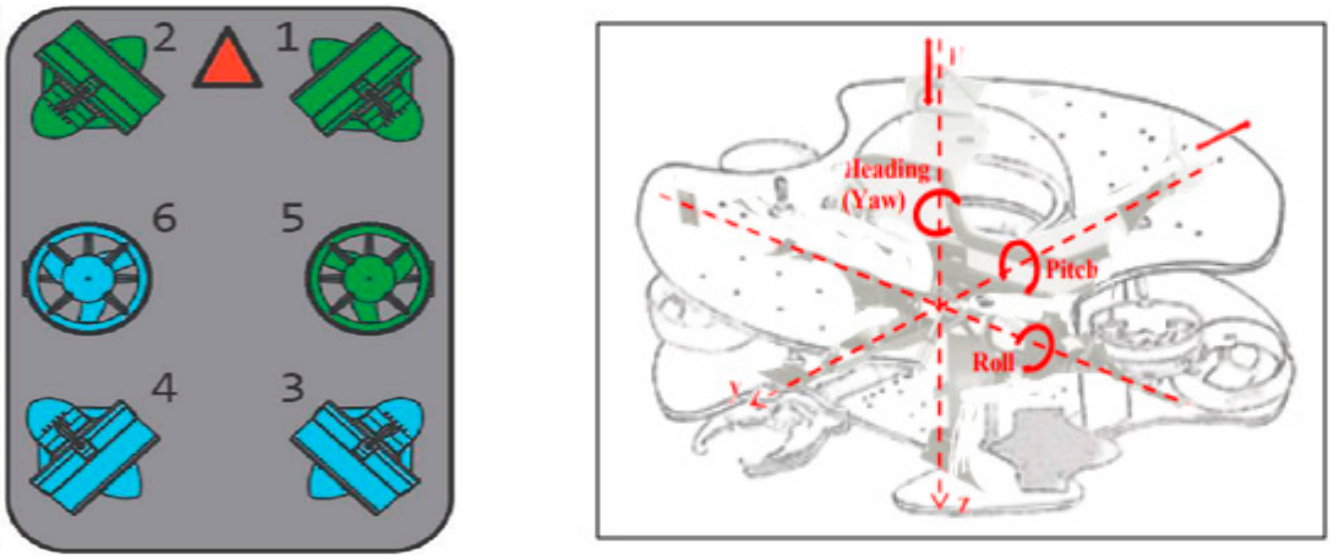

Figure 4. Thruster configuration: (**a**) Motor Positioning [26], (**b**) Motion of ROV in 6-DOF. The red triangle represents the direction of motion.

3.4. Gripper and Camera Enclosure

A pneumatically actuated manipulator was designed to perform underwater tasks successfully. The actuator is a pneumatic cylinder (bore 30 mm and stroke 60 mm). It depends on the mechanism of the parallel link to convert the linear motion of the cylinder to a gripping action. The gripper's jaws were designed especially for the missions as shown in Figure 5a.

(**a**) (**b**)

Figure 5. (**a**) Hydraulics gripper arm, (**b**) camera enclosure.

To perform the tasks appropriately, we set up two cameras to allow the pilot to control the vehicle. The main camera is set in the electronic enclosure and faces the front side of the ROV. The cameras were also used for image processing at the request of our software tasks. The second camera was installed to capture photos of the gripper. The enclosure was made of artelon, with a gland at its end to pass the camera's cable through. An acrylic drum was added to allow the light to pass through for a better vision. The camera enclosure is shown in Figure 5b.

3.5. Stress Analysis

Taking the weight and strength factors into consideration, a stress analysis was conducted to determine the following:

- The maximum pressure that the upper plate and lower plate can withstand.
- The weight effect of the mechanical parts fixed to the upper and lower plates.
- The ability of the electric enclosure to withstand pressure under 7-m depth.

4. Electrical System Design

In terms of electrical design, standards must be set that regulate the electrical circuit. It is important to know the distribution of energy in the ROVs, and to reach an electrical circuit that works with the suitable efficiency and the least capabilities. This section aims to develop a customer-oriented design that would optimize performance while maintaining modularity and flexibility. The electrical system consists of the following primary components: (i) surface control station, (ii) tether system, and (iii) onboard electronics [27]. Figure 6 shows the flowchart of the electrical system integration diagram (SID).

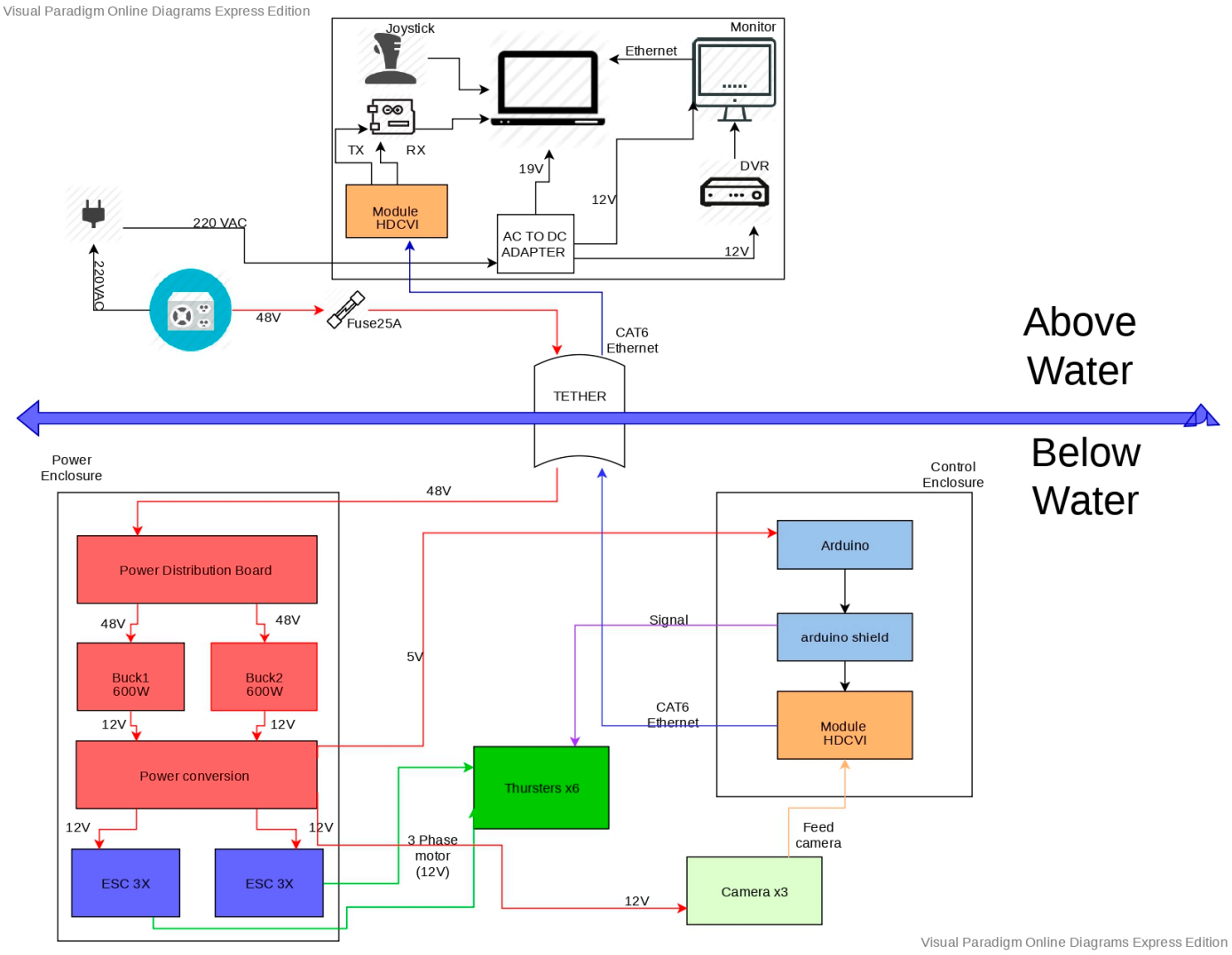

Figure 6. Flowchart of electrical system (SID).

The ROV was controlled from the surface using a laptop and a gaming controller. Firstly, the electrical circuit was drawn as a hand sketch, enabling each component to be placed in the electric circuit, extending each element that needs power. Subsequently, the desired area of the electrical circuit was calculated, and the electrical circuit was modeled using Eagle and Easy EDA software programs, and every part was determined in the electrical circuit as shown in Figure 7.

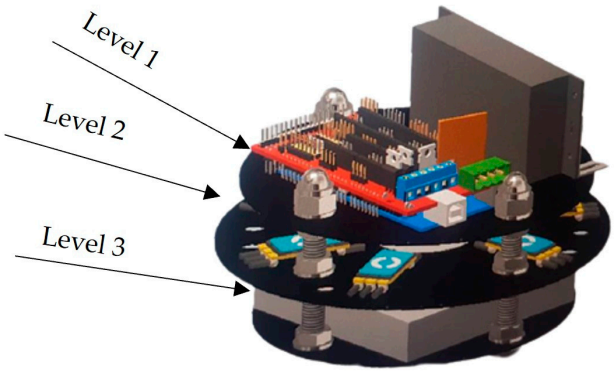

Figure 7. Electical Circuit.

Control data was sent from the Arduino to a passive high-definition composite video interface (HDCVI) transceiver connected by another passive HDCVI transceiver in the ROV's electric enclosure using a Category 6 cable connecting to the onboard Arduino mega through two wires. A Category 6 cable was utilized because it provides high data. Through put for the Ethernet cameras on the ROV. Since Arduino boards already have support circuitry built in, the carrier board design was made simpler by using them throughout the system. Additionally, because of their low cost, it is sometimes simpler and less expensive to replace a whole defective Arduino board rather than isolated components.

A 48 V power supply was delivered to the ROV's PCB using 14 American wire gauge (AWG) wires with an in-line 25-A fuse. The electric enclosure consists of three levels. The first level contains the Power PCB, the second has the electronic speed controller (ESC), and the third includes the Arduino Mega with a shield and a passive HDCVI transceiver. The 48 V enters the Power PCB and is converted to 12 V through the Murata DC-DC converter [28]. Subsequently, the 12 V is distributed by the Power PCB to the ESCs, cameras, and a power converter from 12 V to 5 V to feed the Arduino [3].

4.1. Power Distribution

When all power usages are determined, the adequate DC power supply rating and power distribution are selected [29]. Here, DC was used rather than AC because it is simpler and more accessible for the portable ROV to use power supply by the generator. The total available power is computed as follows:

$$\text{Total available power} = \text{Power supply power} - \text{Tether power loss} \quad (15)$$

The ROV electricity consists of the following components: T100 thruster, ESC, cameras, and Arduino digital video recorder (DVR). Table 1 tabulates the power distribution for each component and the tether power loss due to temperature. The table shows that the power consumption is lower than the available power [2].

Table 1. Power distrubiton.

Component	Quantity	Voltage (V)	Power per Device (W)	Total Power (W)
T100 Thruster	6	12	135	800
ESC	6	12	6	36
Cameras	2	12	6	12
Arduino Mega	1	12	6	6
DVR	1	12	15	15
Total power				879
Tether power loss				230

4.2. Power Board

The track width was estimated using Equation (16):

$$\text{Width} = \text{Area}/\text{Thickness} \times 1.378\ \text{mile}/\text{oz} \quad (16)$$

For every 1 A, 1 mm track width is required for PCB input. Thus, a 30 mm track width is necessary to meet the desired current (30A), resulting in a massive space for the electronics in the electric enclosure [30]. To maintain a smaller track width size, we coated it with a composite mixture of silver, tin, and gold. As the PCB thickness increases, the track decreases. Figure 8 depicts the power board.

The power PCB receives 48 V from the tether and uses 2 Murata DC-DC converters (buck) to convert the 48 V to 12 V with an excellent nominal efficiency of 96% [31]. They were used due to their small size and low weight. Designing the power PCB that can handle the required current in a small size to fit in the electric enclosure was a challenge. After conversion, the 12 V bus was distributed into two buses; the first bus was converted

to 5 V to DC-DC converter, and the second was distributed using terminals to provide the ESCs and the cameras with the required operating power.

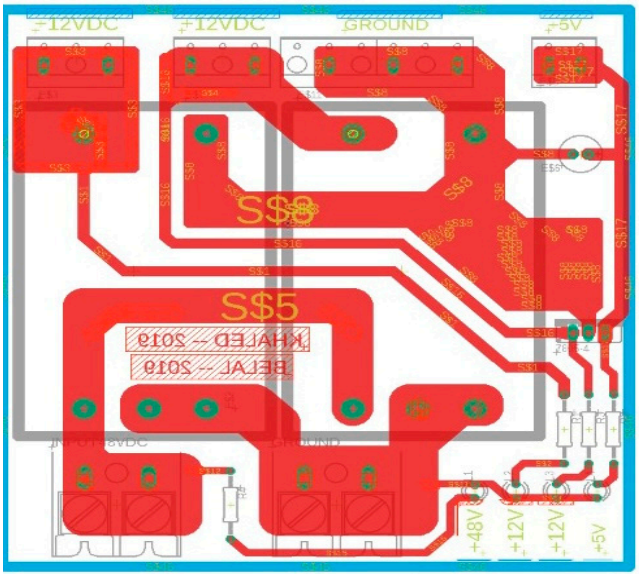

Figure 8. Power board.

4.3. Control Board

The control board was connected to the PCB board, as shown in Figure 9. The control shield was mounted to Arduino. The shield was used to deliver the signals from the Ardunio Mega to the components through terminals to fasten the wires gently and avoid disconnection. The shield contains 20 terminals (7 for the signal, 7 for the ground, and 6 for the small power). A Tether cable was mounted between the vehicle and the tether management system (TMS) for transmitting electrical power, optical signals and mechanical loads using a thin, flexible, and durable cable [31].

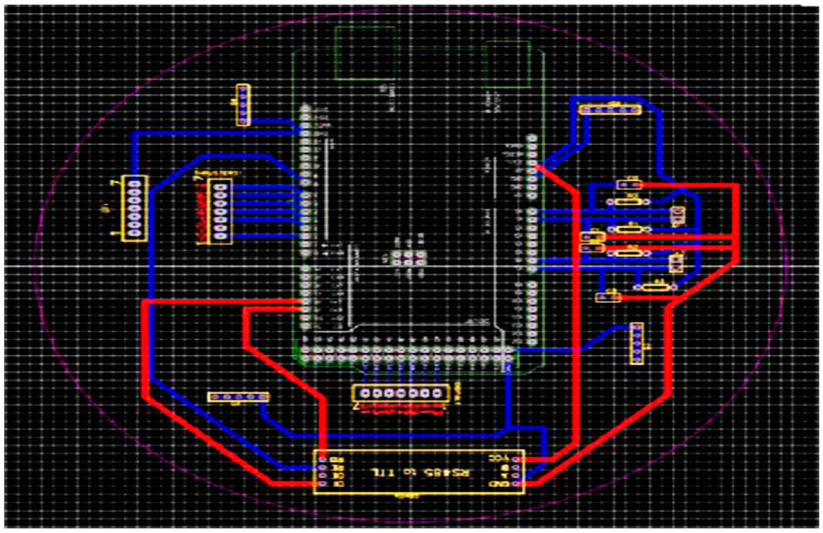

Figure 9. Control board.

5. Software System

The first step of the software system involves the station between the Arduino microcontroller and the joystick. The second step involves the bottom side between the top side Arduino and the bottom side Arduino.

5.1. Top Side System

The station was designed to allow the user to control the system thoroughly. The station consists of a power supply, computer, screen, joystick controller, laptop, and upper Arduino as a controller for the upper control station. The joystick and the upper Arduino (transmitter) were connected to the laptop and was connected to the joystick. The upper Arduino receives the information (i.e., coordinates) from the joystick and transmits it to the bottom Arduino to operate the motors using "Processing IDE". We developed a graphical user interface (GUI) to allow the pilot to control the speed and motion of motors. The top Arduino communicates with the bottom Arduino underneath the water through a universal asynchronous receiver-transmitter (UART) to simplify the process that any of two Arduino can send and receive data from each other.

The purpose of the code in the processing is to handle the top-side system and connects the Logitech extreme with the upper Arduino. The joystick sends the speed to the upper Arduino in a hexadecimal arrangement to save memory since the maximum speed (255 ms) can be saved only in 2 bytes. The upper Arduino receives the speed and sends it through serial communication in a UART cable to the bottom Arduino underneath the water. We used Logitech 3D pro joystick. We programmed Logitech 3D pro joystick using "Processing" and controlled motors using a Proportional-integral-derivative (PID) control PID.

5.2. Bottom Side System

On the bottom side, the underwater software is managed by an Arduino Mega that receives the motor speed and converts it into a decimal system which subscribes to the node that maps the values and drives the thrusters through the ESCs. Accordingly, the motors publish the readings of the sensors responsible for localization. The camera's system transmits the underwater data to the laptop by cat-6 Ethernet cable and passive transverse module for image processing. Figure 10 illustrates the software map.

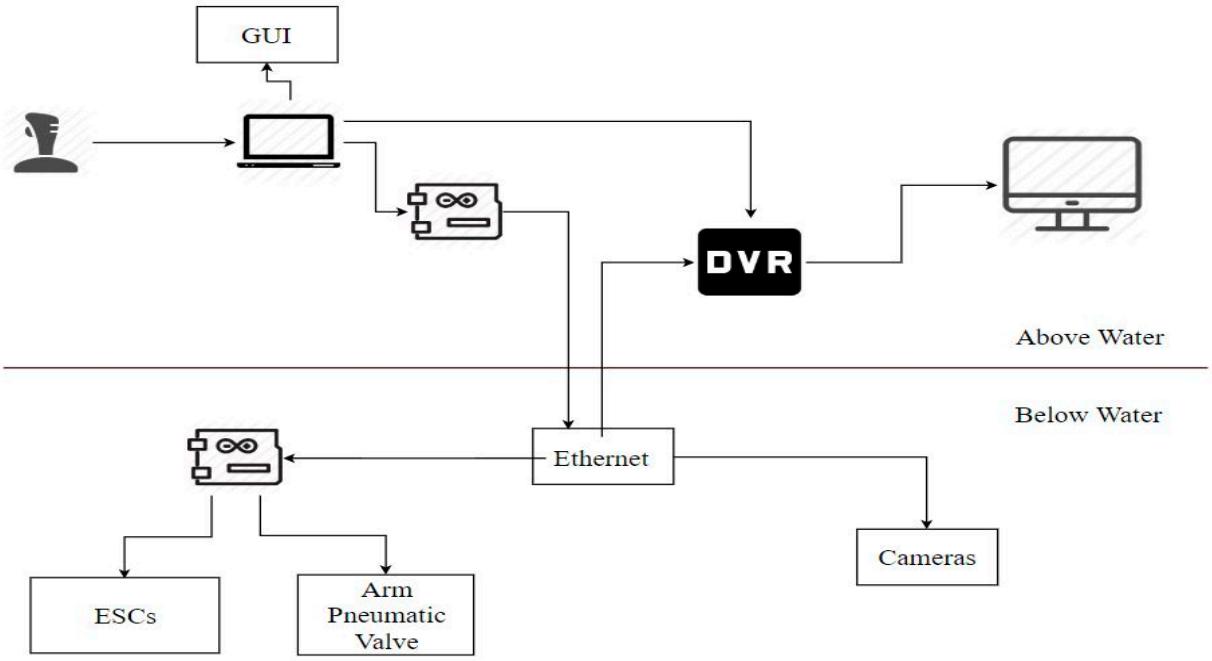

Figure 10. Software map.

5.3. Image Processing

Python was used for image processing because it is open source, has decent documentation, and has a great performance with relatively low-level libraries. Matplotlib and NumPy were used. The process starts with capturing a frame from the camera feed and

saving it to the appropriate directory on the control laptop. Subsequently, several filters (from OpenCV) were applied to compensate for the 'fuzziness' caused by shooting under the water. Eventually, the images become processed.

6. Experimental Setup

The experimental investigation was conducted to test the ROV's applicability to various missions. Prior to submerging ROV in a swimming pool, we ran extensive testing to ensure it would be fully waterproof. We used a vacuum pump to pull a vacuum inside the electronics enclosure, adjusting the seal if there was any sign of pressure change. Next, we covered the enclosure in soapy water and pressurized the interior so that escaping air would create bubbles and be easy to detect. We also allowed the ROV to run for 15 min with the enclosure sealed to ensure that the interior did not get too hot.

The dimensions of the enclosed swimming pool used in the experimental investigation are 25 × 20 × 7 m (Figure 11). First, the objects required for performing the missions of ROV are placed in the swimming pool. To ensure the insulation of the electrical enclosure, the ROV was tied with a rope and left underwater for twenty minutes without activating the power. Subsequently, the pilot activates the power and uses the joystick to control the vehicle in the desired direction through the GUI platform. During the experiment, the installed cameras allow the pilot to display the desired objects on the laptop.

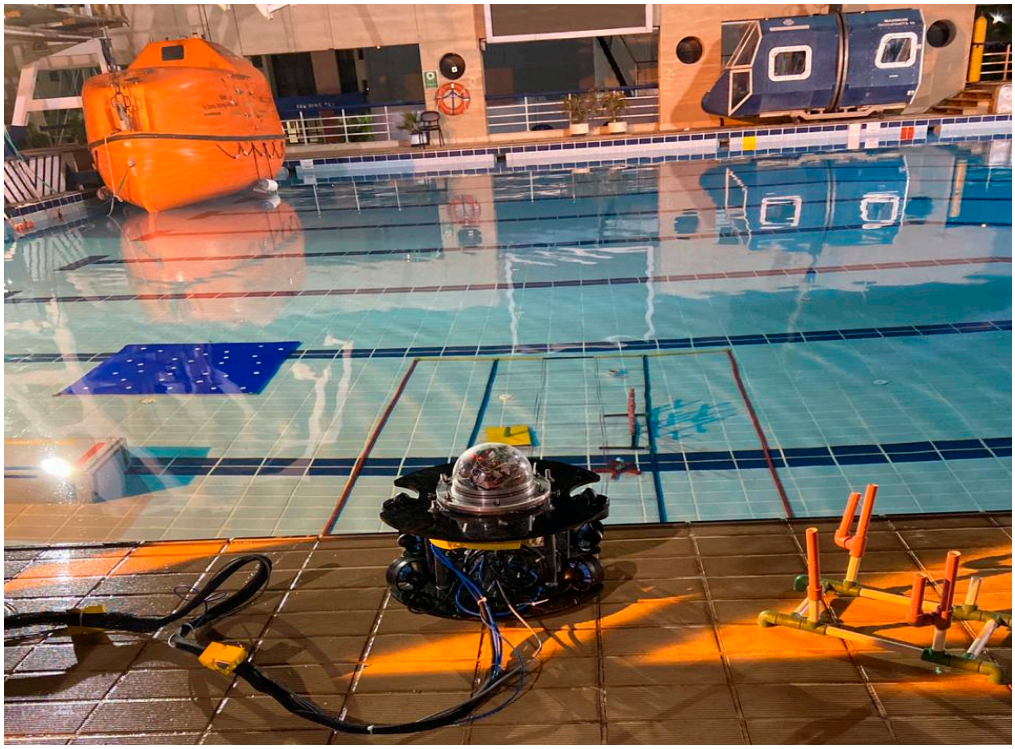

Figure 11. Experimental setup.

7. Results and Discussion

A circular-shaped underwater ROV, which allows the utilization of six thrusters to enhance the maneuverability and controllability of the vehicle by six DOF was fabricated. Figures 12 and 13 show the final manufactured PCB and underwater ROV prototype, respectively. Table 2 tabulates the key specifications of the proposed ROV. The maximum speed and weight of the proposed ROV are in line with the recent findings reported by Ali et al. [9].

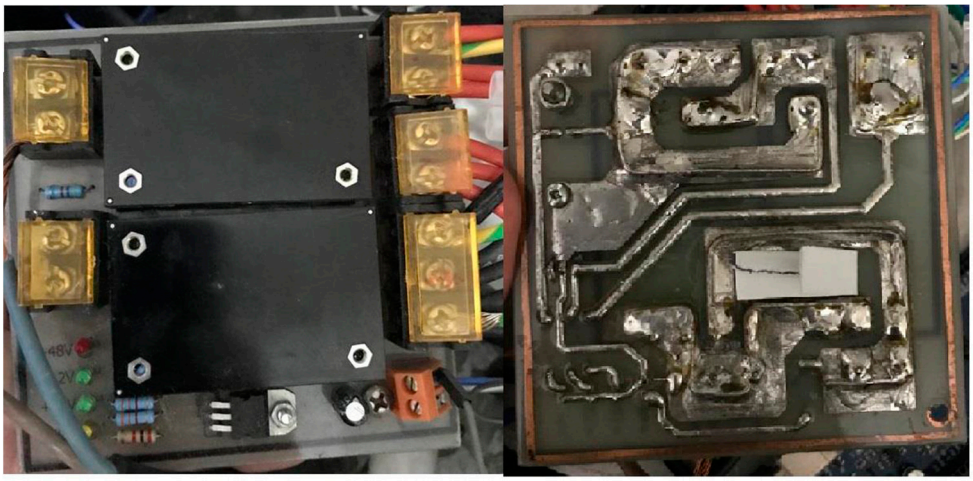

Figure 12. Proposed PCB.

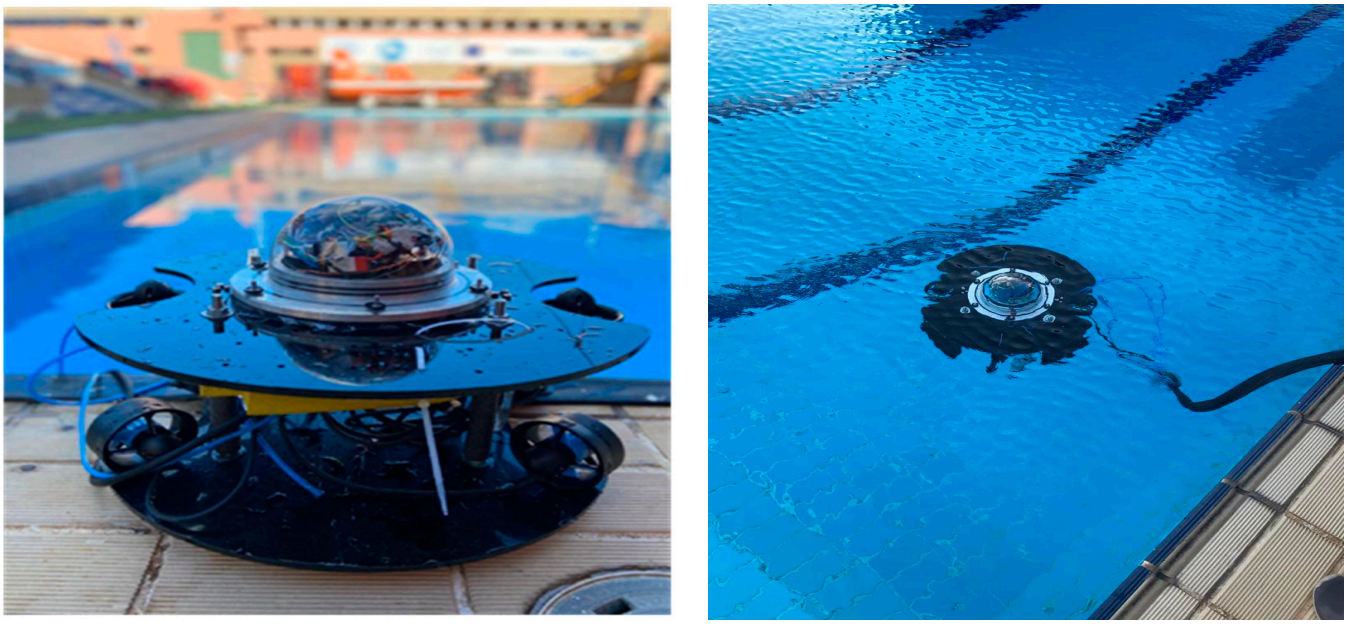

Figure 13. ROV prototype.

Table 2. Main specifications of the developed ROV.

Parameter	Value	Unit
Maximum speed	4.86	km/h
Maximum depth	7	m
Maximum current	30	A
Weight	16	kg
Size	46 × 64 × 55	cm
PCB size	10 × 10	cm
Life in water	3	h
Track width mixture	60% tin, 30% silver, and 10% gold	-

7.1. Stress Analysis

According to the stress analysis in Figure 14, the acrylic upper and lower plates and electric enclosure could withstand the pressure forces acting on them. Table 3 presents the actual stress and strain results for each component.

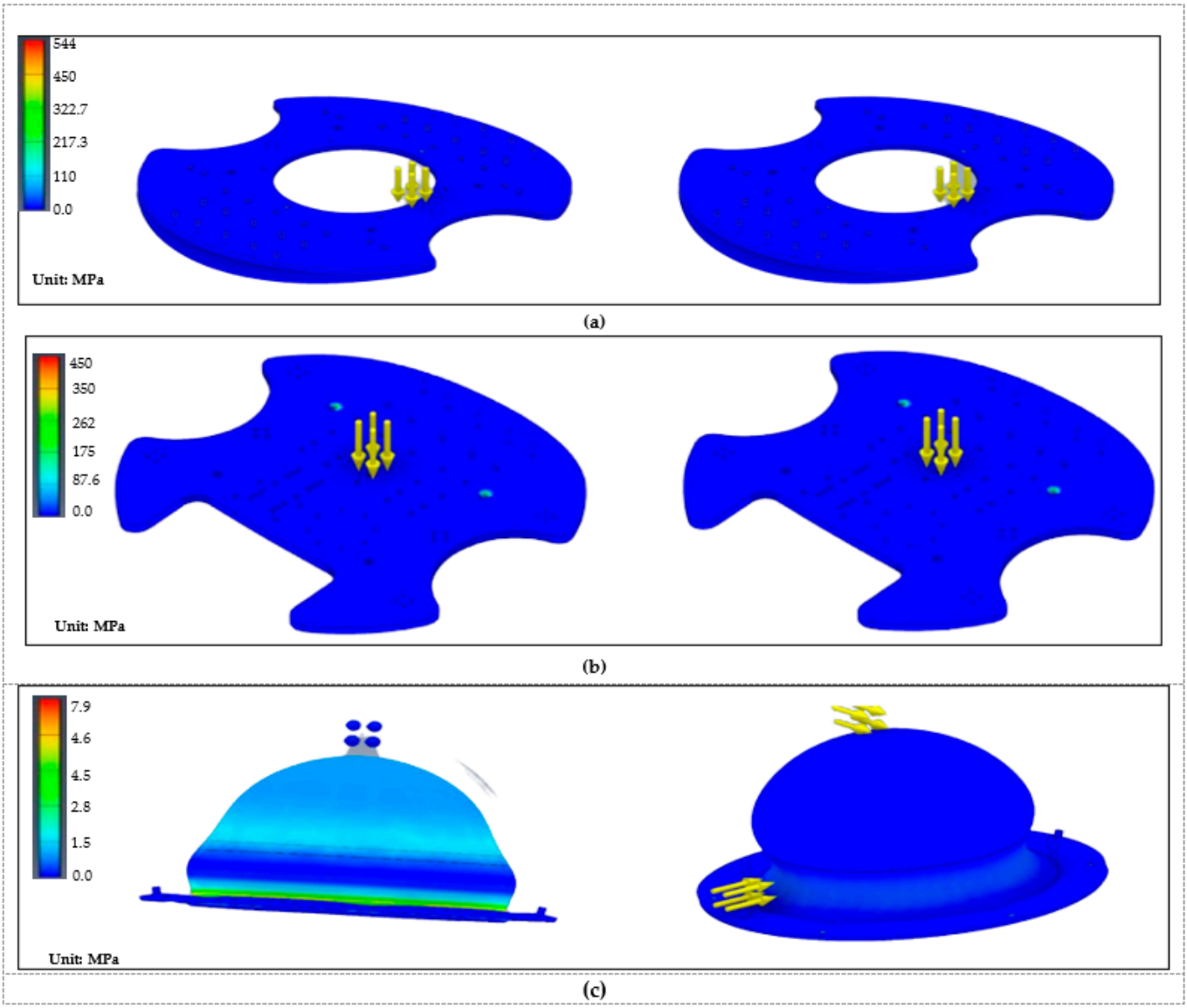

Figure 14. Stress analysis: (**a**) upper plate, (**b**) lower plate, (**c**) electric enclosure.

Table 3. Stress and strain results of the ROV parts.

Part	Min. Stress (MPa)	Max. Stress (MPa)	Min. Strain	Max. Strain
Upper Plate	0	0.2	0.0	0.010
Lower plate	0	70.0	0.0	0.030
Electrical Enclosure	0	2.5	0.0	0.001

7.2. Proposed GUI Platform

The top side platform consists of a GUI screen for the pilot and co-pilot to observe the motors' conditions, movements, and speeds. Figure 15 depicts the proposed GUI. The GUI allows the pilot to move the six-DOF ROV movement of six motors using LEFT, RIGHT and ELEV boxes. Moreover, it pares the rotation movement and ROV transfer in line with a recent study [2].

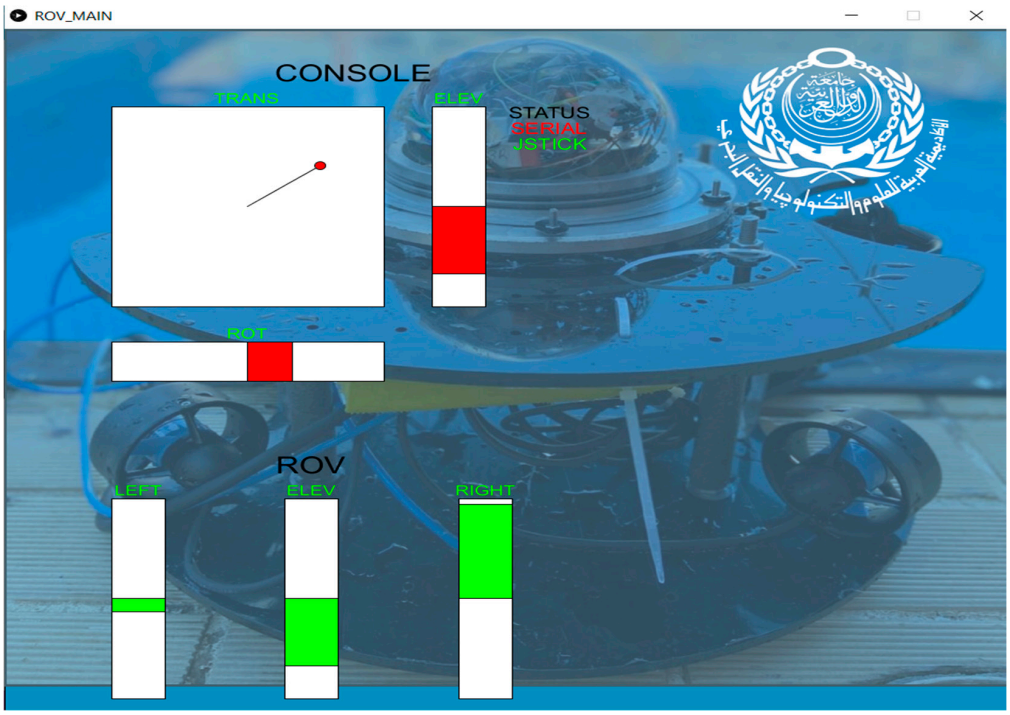

Figure 15. Proposed GUI.

7.3. Image Recognition

7.3.1. Red Line Follower

To autonomously follow the transect line, the forward-facing closed-circuit television (CCTV) camera image was masked to filter out everything except the red line, as shown in Figure 16. The algorithm computes a motion vector based on the location of readings right, left, up, and down, depending on the direction in which the red color appears. The line in the image and the opposite direction of motion keep the ROV centered on the line in either the horizontal or vertical axis.

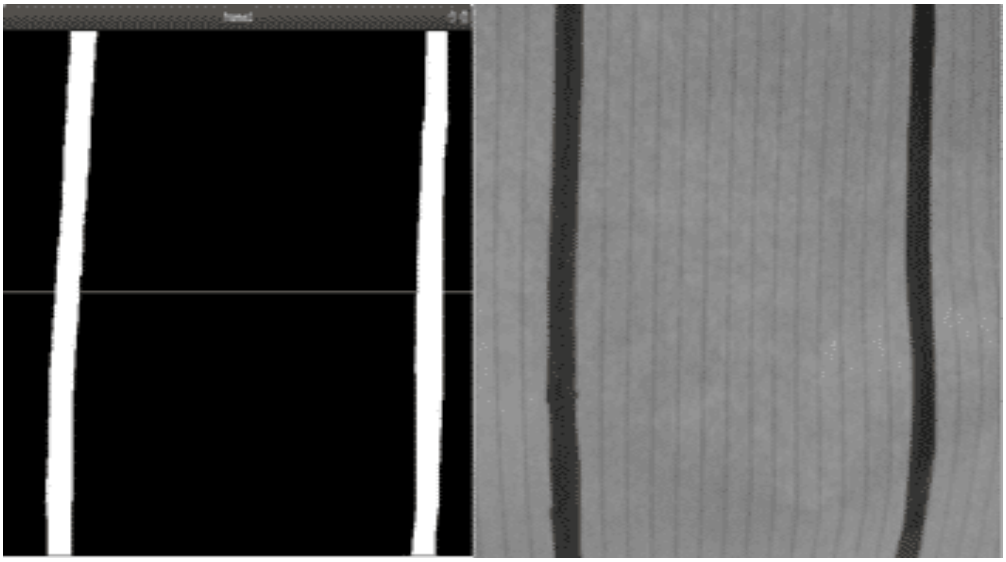

Figure 16. Red line follower test (the underwater red lines appear grey on the right).

7.3.2. Blue Crack Detection

This test aims to detect a certain crack with a pre-defined width and compute the crack length. The crack is represented by a blue line which is detected and measured using Python and the open-source computer vision library OpenCV. The crack detection algorithm masks the image from the CCTV camera and allows the user to display the crack on the laptop. Here, we used a reference line with an actual length of 14.318 cm and a width ranging between 1.8 and 1.9 cm. The pixels are identified for the blue line and the crack length L_{cr} is evaluated based on Equation (17). Figure 17 illustrates the detected blue line in the swimming pool. In this test, evaluated L_{cr} was 13.38 cm, with an accuracy of 93%:

$$L_{cr} = W_{ref}\left(\frac{L_p}{W_p}\right) \tag{17}$$

where W_{ref} is the reference width in cm, L_p is the length of the blue line in pixels, and W_p is the width of the blue line in pixels.

Figure 17. Crack length detection test. The blue line represents the crack.

7.3.3. Identifying Benthic Species

This test aims to identify stationary benthic species represented by various shapes, such as lines, polygons, and circles. Python uses OpenCV to construct a computer vision system to quickly identify, count, and categorize multiple species. The algorithm seeks each shape's contours (i.e., lines representing boundaries) and highlights them. Subsequently, the shape is identified by counting the vertices of each contour. For example, a shape is recognized as a triangle if it has three vertices. Figure 18 demonstrates a sample of the benthic species identification through image processing. Here, the image processing first identified the different shapes of benthic species (Figure 18a), then counted the number of species according to the defined shapes (Figure 18b).

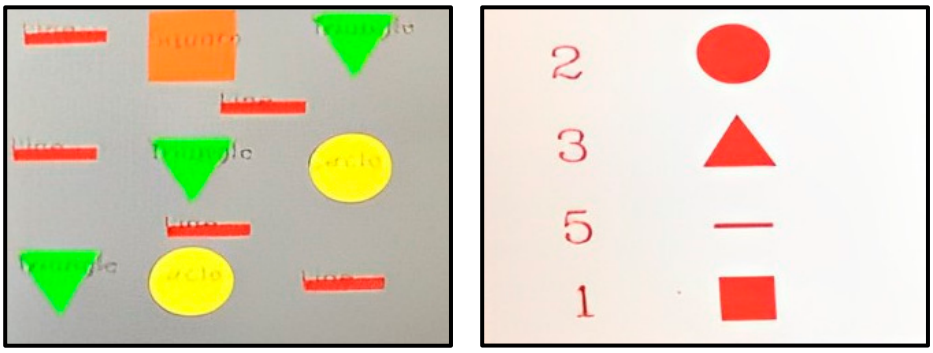

(**a**) (**b**)

Figure 18. Benthic species test: (**a**) identification of benthic species shapes; (**b**) evaluation of benthic species count.

7.3.4. Analyzing Box Sides

The five sides of any underwater obstacle are analyzed to perform this task. Accordingly, the obstacles are simulated using boxes with different colors, as shown in Figure 19c. The range of the camera will be minimized to match the size of every side of the box; for instance, the frame range of the camera will be 1100 × 500 pixels for one side, and for another side, it will be 500 × 500, and so on. Subsequently, a screenshot is taken for every side of the box (Figure 19b). Eventually, the screenshots will be arranged in the proper form as shown in Figure 19a.

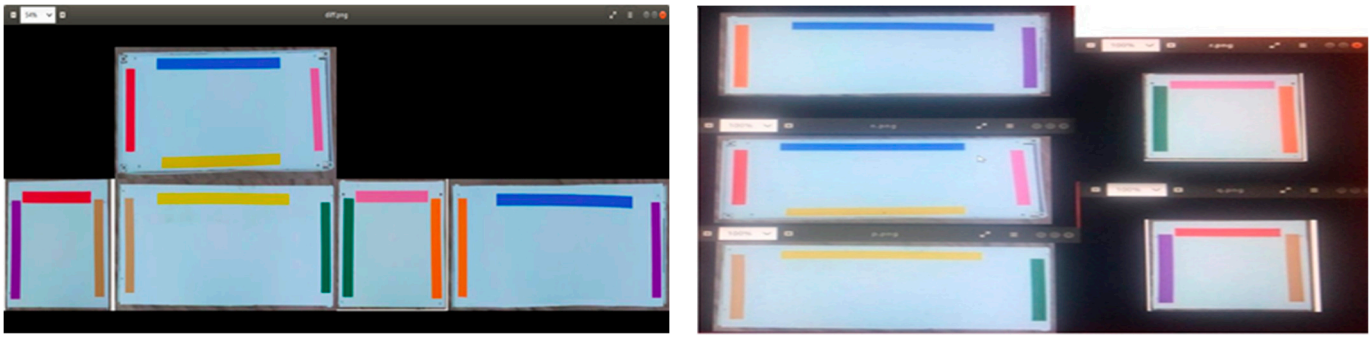

(**a**) (**b**)

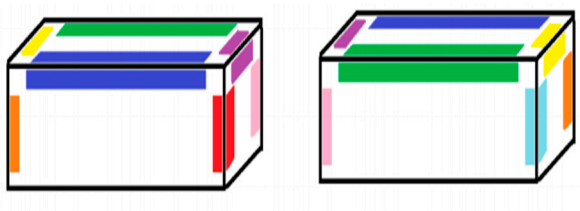

(**c**)

Figure 19. Analyzing obstacles: (**a**) analyzing box sides, (**b**) analyzing every box side individually, (**c**) analyzing boxes with different colors.

8. Conclusions

In this paper, we developed an integrated system for an underwater ROV that considers mechanical, electrical, and software design and manufacturing. The PCB was designed with a small track width to reduce the ROV's overall dimensions. All independent systems of the proposed ROV were tested individually before assembly to ensure they were fully operational and ready for integration. The vehicle's structural integrity and insulation were examined by submerging the vehicle underwater for long periods. The experimental

outcomes demonstrate the image processing's robustness in performing various tasks in underwater environments.

In the current investigation, the allowable depth was limited to 7 m. Thus, researchers could consider using autonomous underwater vehicles to explore greater depths in future work. The present study did not consider shape analysis; accordingly, the corresponding theoretical and experimental research regarding shape selection was insufficient to present significant findings. Thus, we recommended the investigation of the ROV's shape on its performance and hydrodynamics in future work. This could be achieved through shape optimization, considering the various operational scenarios. Moreover, computer vision applications could be integrated to develop the capability of ROVs to identify benthic species under hazardous and unstable conditions.

Author Contributions: Conceptualization, K.M.S., H.A. and H.E.; methodology, K.M.S. and H.A.; software, K.M.S.; validation, K.M.S., H.A. and H.E.; formal analysis, K.M.S.; investigation, K.M.S.; resources, K.M.S., H.A., H.E. and M.R.; data curation, K.M.S.; writing—original draft preparation, K.M.S. and M.R.; writing—review and editing, K.M.S., H.A. and M.R.; visualization, K.M.S., H.A. and M.R.; supervision, H.A. and H.E.; project administration, H.E. All authors have read and agreed to the published version of the manuscript.

Funding: This research received no external funding.

Institutional Review Board Statement: Not applicable.

Informed Consent Statement: Not applicable.

Data Availability Statement: The data presented in this study are available upon reasonable request from the corresponding author.

Conflicts of Interest: The authors declare no conflict of interest.

References

1. Elangovan, M.; Yuvan, S.B.; Uduupa, G.R.; Babu, M.M. Design and Development of Underwater ROV for Dam Inspection. *Res. Sq.* **2022**. [CrossRef]
2. Kabanov, A.; Kramar, V.; Ermakov, I. Design and Modeling of an Experimental Rov with Six Degrees of Freedom. *Drones* **2021**, *5*, 113. [CrossRef]
3. Brundage, H.M.; Cooney, L.; Huo, E.; Lichter, H.; Oyebode, O.; Sinha, P.; Stanway, M.J.; Stefanov-Wagner, T.; Stiehl, K.; Walker, D. Design of an ROV to Compete in the 5th Annual MATE ROV Competition and Beyond. In Proceedings of the OCEANS 2006, Boston, MA, USA, 18–21 September 2006; pp. 1–5.
4. Vu, M.T.; Le, T.-H.; Thanh, H.L.N.N.; Huynh, T.-T.; Van, M.; Hoang, Q.-D.; Do, T.D. Robust Position Control of an Over-Actuated Underwater Vehicle under Model Uncertainties and Ocean Current Effects Using Dynamic Sliding Mode Surface and Optimal Allocation Control. *Sensors* **2021**, *21*, 747. [CrossRef] [PubMed]
5. Last, G.; Williams, P. *An Introduction to ROV Operations*; Oilfield Publications, Incorporated: New York, NY, USA, 1991; ISBN 1870945239.
6. Christ, R.D.; Wernli Sr, R.L. *The ROV Manual: A User Guide for Remotely Operated Vehicles*; Butterworth-Heinemann: Oxford, UK, 2013; ISBN 0080982913.
7. Shimono, S.; Matsubara, O.; Toyama, S.; Nishizawa, U.; Kato, S.; Arisumi, H. Development of Underwater Inspection System for Dam Inspection. In Proceedings of the OCEANS 2015—MTS/IEEE Washington, Washington, DC, USA, 19–22 October 2015; pp. 1–6.
8. Gould, R.A. *Archaeology and the Social History of Ships*; Cambridge University Press: Cambridge, UK, 2011; ISBN 9780521194921.
9. Ali, Z.A.; Li, X.; Tanveer, M.A. Controlling and Stabilizing the Position of Remotely Operated Underwater Vehicle Equipped with a Gripper. *Wirel. Pers. Commun.* **2021**, *116*, 1107–1122. [CrossRef]
10. Armstrong, R.A.; Pizarro, O.; Roman, C. Underwater Robotic Technology for Imaging Mesophotic Coral Ecosystems. In *Mesophotic Coral Ecosystems*; Springer: Cham, Switzerland, 2019; pp. 973–988.
11. Ali, Z.A.; Li, X.; Noman, M. Stabilizing the Dynamic Behavior and Position Control of a Remotely Operated Underwater Vehicle. *Wirel. Pers. Commun.* **2021**, *116*, 1293–1309. [CrossRef]
12. Dong, M.; Li, J.; Chou, W. Depth Control of ROV in Nuclear Power Plant Based on Fuzzy PID and Dynamics Compensation. *Microsyst. Technol.* **2020**, *26*, 811–821. [CrossRef]
13. Bykanova, A.Y.; A Storozhenko, V.; Tolstonogov, A.Y. The Compact Remotely Operated Underwater Vehicle with the Variable Restoring Moment. *IOP Conf. Ser. Earth Environ. Sci.* **2019**, *272*, 022199. [CrossRef]
14. Omerdic, E.; Toal, D.; Dooly, G. Precision Control and Dynamic Positioning of ROVS in Intervention Operations. *J. Robot Autom.* **2017**, *1*, 24–41.

15. He, Y.; Wang, D.B.; Ali, Z.A. A review of different designs and control models of remotely operated underwater vehicle. *Meas. Control.* **2020**, *53*, 1561–1570. [CrossRef]
16. Van de Ven, P.W.J.; Flanagan, C.; Toal, D. Neural Network Control of Underwater Vehicles. *Eng. Appl. Artif. Intell.* **2005**, *18*, 533–547. [CrossRef]
17. Caccia, M.; Veruggio, G. Guidance and Control of a Reconfigurable Unmanned Underwater Vehicle. *Control. Eng. Pract.* **2000**, *8*, 21–37. [CrossRef]
18. Do, K.D.; Pan, J.; Jiang, Z.-P. Robust and Adaptive Path Following for Underactuated Autonomous Underwater Vehicles. *Ocean. Eng.* **2004**, *31*, 1967–1997. [CrossRef]
19. Hoang, N.Q.; Kreuzer, E. Adaptive PD-Controller for Positioning of a Remotely Operated Vehicle Close to an Underwater Structure: Theory and Experiments. *Control. Eng. Pract.* **2007**, *15*, 411–419. [CrossRef]
20. Vu, M.T.; Choi, H.-S.; Nhat, T.Q.M.; Ji, D.-H.; Son, H.-J. Study on the Dynamic Behaviors of an USV with a ROV. In Proceedings of the OCEANS 2017-Anchorage, Anchorage, AK, USA, 18–21 September 2017; pp. 1–7.
21. Fossen, T.I. *Handbook of Marine Craft Hydrodynamics and Motion Control*; John Wiley & Sons: Hoboken, NJ, USA, 2011; ISBN 1119991498.
22. Fossen, T. *Guidance and Control of Ocean Vehicles*; John Willey & Sons. Inc.: New York, NY, USA, 1994.
23. Bai, Y.; Bai, Q. *Subsea Engineering Handbook*; Gulf Professional Publishing: Houston, TX, USA, 2018.
24. Features GitBook. Available online: https://www.ardusub.com/introduction/features.html (accessed on 11 December 2022).
25. T100 Thruster Core. Available online: https://bluerobotics.com/store/thrusters/t100-t200-thrusters/t100-thruster-core/ (accessed on 6 December 2022).
26. Capocci, R.; Dooly, G.; Omerdić, E.; Coleman, J.; Newe, T.; Toal, D. Inspection-Class Remotely Operated Vehicles—A Review. *J. Mar. Sci. Eng.* **2017**, *5*, 13. [CrossRef]
27. Bogue, R. Underwater Robots: A Review of Technologies and Applications. *Ind. Robot. Int. J.* **2015**, *42*, 3. [CrossRef]
28. Isolated DC-DC Converter | Power Products | Product Search | Murata Manufacturing Co., Ltd. Available online: https://www.murata.com/search/productsearch?cate=cgsubPowerIsoDcDc (accessed on 11 December 2022).
29. Tamam, B.; Mardiyanto, R. Development of Water-Surface Robotic Vehicle to Assist Communication Between Remotely Operated Vehicle Underwater Robot and Control Station. *JAREE* **2017**, *1*, 2. [CrossRef]
30. Armstrong, M.K. PCB design techniques for lowest-cost EMC compliance. Part 1. *Electron. Commun. Eng. J.* **1999**, *11*, 185–194. [CrossRef]
31. Martos, G.; Abreu, A.; Gonzalez, S.; Tremante, A. *Remotely Operated Underwater Vehicle (ROV) 100% Report*; Florida International University: Miami, FL, USA, 2013.